


Large Switchable Circular Photogalvanic Effect in the Narrow-Band-Gap InSe/In₂Se₃ Ferroelectric Heterojunction

Guoli Lin, Yiqun Xie[✉],* Li Shu, and Xiang Ye

Department of Physics, Shanghai Normal University, 100 Guilin Road, Shanghai 200234, People's Republic of China

 (Received 24 April 2023; revised 20 July 2023; accepted 22 August 2023; published 15 September 2023)

The photogalvanic effect in ferroelectric (FE) materials attracts considerable interest in solar cells, polarization-sensitive photodetection, and nonvolatile memory applications. However, narrow-band-gap FE materials that cover the full solar spectrum are currently rare, and there is still room to enhance the light-polarization sensitivity and to improve the switching ratio for FE optoelectronic devices. Here, we investigate the photogalvanic effect induced by elliptically polarized light in the narrow-band-gap (< 1.6 eV) InSe/In₂Se₃ FE heterojunction (HJ) stacked with the InSe monolayer and α -In₂Se₃ FE monolayer. The dependence of the photocurrent on the polarization angle, ϕ , and on the incidence angle, α , is formulated within the nonequilibrium Green's function formalism, with which the photocurrent is then calculated by using first-principles methods. We find that both the linear photogalvanic effect (LPGE) and circular photogalvanic effect (CPGE) are generated from the infrared to the visible range. The CPGE is only induced at oblique incidence due to C_{3v} symmetry of the HJ and can be 10^3 times larger than the LPGE. The largest photocurrent is achieved when light is irradiated along the zigzag direction, which is dominated by the CPGE. The photocurrent can further be tuned by switching between upward and downward FE polarization, leading to a large switching ratio of 563. The photocurrent also shows an excellent light-polarization sensitivity at normal and oblique incidence, with an impressive extinction ratio of 410. These results shed light on the CPGE of FE materials for applications in low-dimensional FE optoelectronics.

DOI: [10.1103/PhysRevApplied.20.034035](https://doi.org/10.1103/PhysRevApplied.20.034035)

I. INTRODUCTION

The photogalvanic effect (PGE) [1–6], namely, the bulk photovoltaic effect [7–15] in ferroelectric (FE) materials, has attracted significant attention because of potential applications in various fields, including solar cells [16–21], photodetection [22–26], nonvolatile memory [27,28], and terahertz-wave generation [29]. The PGE occurs in materials without space-inversion symmetry and generates a persistent photocurrent under illumination from polarized light without the need for an external bias or built-in electric field. Moreover, the PGE can produce a large open-circuit photovoltage that is much greater than the band gap [17], making it promising for exceeding the Shockley-Queisser limit in traditional p - n solar cells. For example, it was reported that the energy-conversion efficiency of the PGE in FE BaTiO₃ exceeded the Shockley-Queisser limit by about 2 times with an open-circuit voltage of 8 V [18]. Additionally, large open-circuit voltages induced by the PGE were also achieved in several other FE materials, including Pb(Zr, Ti)O₃ (6.60 V) [19], BiFeO₃ (9.66 V) [20], and BaTiO₃-based

ferroelectric oxides (7.39 V) [21]. However, most FE materials have a larger band gap, such as BaTiO₃ (3.5 eV) [30], Pb(Zr, Ti)O₃ (3.6 eV) [31], BiFeO₃ (2.7 eV) [32,33], and CuInP₂S₆ (2.9 eV) [34]. Such a large band gap means that only 8%–20% of the visible-light spectrum can be absorbed, which severely hinders their practical applications. Therefore, narrow-band-gap FE materials (< 1.6 eV) that cover the whole visible range are desirable for solar cells.

The PGE in FE materials also enables self-powered and light-polarization-sensitive photodetection, since the PGE photocurrent is intrinsically dependent on light polarization. For example, experiments have shown that the two-dimensional (2D) Dion-Jacobson-type FE photodetector demonstrates a polarization sensitivity with an extinction ratio of 4.8 [23], and the 2D hybrid perovskite (allylammonium)₂(ethylammonium)₂Pb₃Br₁₀ FE photodetector possesses a larger extinction ratio of 15 [24]. However, compared to nonferroelectric photodetectors, there is still considerable room to improve the light-polarization sensitivity. For instance, a high extinction ratio of 288 has been reported for a black-phosphorous-based photodetector [35]. Furthermore, the PGE in FE materials can be modulated by reversing the direction of FE polarization

*yqxie@shnu.edu.cn

to change the photocurrent, leading to a large switching ratio. Experiments have shown that, by reversing the FE polarization of $\text{Pb}(\text{Zr}, \text{Ti})\text{O}_3$, the PGE photocurrent can be significantly changed, with a larger switching ratio of 22, which is acceptable in many practical applications, such as nonvolatile memory [28]. Therefore, it is of practical importance to further enhance the switching ratio of the PGE in FE materials.

For the PGE in FE materials, most studies have focused on the linear photogalvanic effect (LPGE), which is generated by linearly polarized light [29,36–38], in which the shift current [9] plays a dominant role. A recent experiment has explored the circular photogalvanic effect (CPGE) in FE BiFeO_3 thin films and suggested that the CPGE can be stronger than the LPGE, as the CPGE generates a larger open-circuit voltage than the LPGE [39]. In fact, previous experiments have already demonstrated that, in the nonferroelectric GaN/AlGaN heterojunction (HJ), the CPGE photocurrent is 1.4 times larger than that of the LPGE [40,41]. These experiments indicate that the CPGE in FE materials deserves further study, as it can produce a larger photocurrent (photovoltage) than the LPGE, which is beneficial for practical applications.

Recently, monolayer $\alpha\text{-In}_2\text{Se}_3$ was proposed to be a FE semiconductor, with both in-plane and out-of-plane ferroelectricity [42–45]; this was then confirmed in experiments by room-temperature ferroelectricity [46]. The LPGE was recently predicted in bilayer $\alpha\text{-In}_2\text{Se}_3$ by using quantum transport simulations based on the nonequilibrium Green's function formalism (NEGF) combined with density-functional theory (DFT) [47]. Additionally, we proposed a vertical HJ stacked with the $\alpha\text{-In}_2\text{Se}_3$ FE monolayer and the InSe nonferroelectric monolayer [48]. This FE HJ has a type-II band alignment with a narrow band gap (< 1.60 eV) and good optical absorption from the infrared to the visible range, which is tunable by switching the FE polarization in the In_2Se_3 monolayer [49], according to first-principles calculations. This indicates that the 2D $\text{InSe}/\text{In}_2\text{Se}_3$ FE HJ is an attractive candidate for exploring the CPGE over the whole visible range.

Here, we study the PGE in the 2D $\text{InSe}/\text{In}_2\text{Se}_3$ HJ by using quantum transport simulations based on the NEGF-DFT method. The HJ belongs to the C_{3v} point group without space-inversion symmetry, and therefore, both the CPGE and LPGE can be generated under the oblique illumination of elliptically polarized light at zero bias. The CPGE photocurrent can be 10^2 to 10^3 times larger than that of the LPGE over a wide visible range. By reversing the FE polarization direction of the In_2Se_3 monolayer, the photocurrent can be tuned with a large switching ratio of up to 563. Moreover, the photocurrent shows a very high polarization sensitivity with an extinction ratio of up to 410. Our results indicate that the FE $\text{InSe}/\text{In}_2\text{Se}_3$ HJ has promising applications in 2D optoelectronics, such as photodetectors, nonvolatile memory, and solar cells.

II. MODEL AND METHODS

The vertical $\text{InSe}/\text{In}_2\text{Se}_3$ FE HJ is constructed by using a lattice constant of 4.06 \AA optimized with the DFT package DS-PAW [50]. This lattice constant is closer to those of the In_2Se_3 monolayer (4.105 \AA) and the InSe monolayer (4.095 \AA), which are also consistent with previous calculations [43,51]. The FE HJ has a hexagonal unit cell with noncentrosymmetric C_{3v} symmetry, as shown in Fig. 1(a). The stacking patterns of the HJ are also illustrated in Figs. 1(b) and 1(c), where the FE polarization of the In_2Se_3 monolayer is downward and upward, respectively. For convenience, we name these two HJs $\text{InSe}/\text{In}_2\text{Se}_3(\downarrow)$ and $\text{InSe}/\text{In}_2\text{Se}_3(\uparrow)$, respectively.

The electronic band structures of the $\text{InSe}/\text{In}_2\text{Se}_3$ HJs are also calculated with the DS-PAW package. The plane-wave basis set with the projector-augmented-wave (PAW) pseudopotential is adopted [52]. The exchange-correlation potentials are approximated using the generalized-gradient-approximation functional as parametrized by the Perdew, Burke, and Ernzerhof (PBE) functional [53]. Since the PBE functional always underestimates the

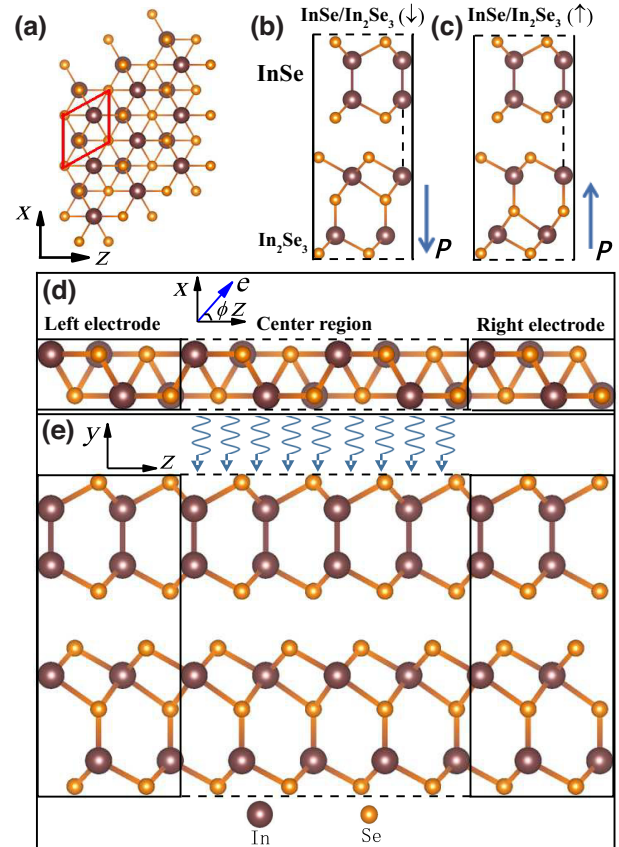


FIG. 1. (a) Top view of the $\text{InSe}/\text{In}_2\text{Se}_3(\downarrow)$ FE HJ, where the primitive unit cell is indicated by a red parallelogram. (b),(c) Side views of the $\text{InSe}/\text{In}_2\text{Se}_3(\downarrow)$ and $\text{InSe}/\text{In}_2\text{Se}_3(\uparrow)$ HJs, respectively. (d),(e) Top and side views of the device model for the $\text{InSe}/\text{In}_2\text{Se}_3(\downarrow)$ HJ, respectively.

semiconductor band gap, the Heyd-Scuseria-Ernzerhof (HSE06) hybrid functional is also used to recalculate the band structure [54]. The DFT-D3 method proposed by Grimme *et al.* is used to describe the van der Waals interaction between the vertical heterojunction layers [55]. Brillouin-zone integration is performed with a $15 \times 1 \times 15$ mesh of Monkhorst-Pack k points for geometry optimization and self-consistent electronic structure calculations. The kinetic energy cutoff for the plane-wave basis is 500 eV. All the atoms in the unit cell are fully relaxed until the force on each atom is less than 0.001 eV/\AA , and the convergence criterion for energy in the self-consistent field cycle is 10^{-5} eV . The climbing-image nudged-elastic-band (NEB) method is used to calculate the kinetics pathways between the two HJs [56].

To study the CPGE and LPGE in the HJs, we construct a device model, as shown in Figs. 1(d) and 1(e). The HJ is divided into three parts, namely, the left and right electrodes and a central region. The entire device is located in the x - z plane, and 20-\AA vacuum layers are added in the y direction to eliminate interactions between periodic image units. The whole device is periodical in the x direction, and the two electrodes are extended into $z = \pm\infty$. The center region is irradiated by elliptically polarized light, and the PGE can be generated with a persistent photocurrent at zero bias voltage due to C_{3v} symmetry. The center region contains four unit cells with a length of 14.02 \AA . We check our results with a larger center region containing six unit cells (21.03 \AA) and find that the main results do not change qualitatively.

Based on the linear response theory [57,58], we have developed a method to calculate the PGE photocurrent in a device based on the NEGF method [59]. Specifically, for elliptically polarized light, the photocurrent injecting into the left electrode can be written as [60,61]

$$J_L^{(\text{ph})} = \frac{ie}{h} \int \left\{ \cos^2 \phi \text{Tr} \left\{ \Gamma_L \left[G_1^{<(\text{ph})} + f_L \left(G_1^{>(\text{ph})} - G_1^{<(\text{ph})} \right) \right] \right\} + \sin^2 \phi \text{Tr} \left\{ \Gamma_L \left[G_2^{<(\text{ph})} + f_L \left(G_2^{>(\text{ph})} - G_2^{<(\text{ph})} \right) \right] \right\} + \frac{\sin(2\phi)}{2} \text{Tr} \left\{ \Gamma_L \left[G_3^{<(\text{ph})} + f_L \left(G_3^{>(\text{ph})} - G_3^{<(\text{ph})} \right) \right] \right\} \right\} dE, \quad (1)$$

where $G_{1,2,3}^{>(<)(\text{ph})}$ denotes the greater (lesser) Green's functions with electron-photon interactions, which are determined by the photon frequency, polarization vector \mathbf{e} , and material symmetry. For elliptically polarized light, the polarization vector is $\mathbf{e} = \cos \phi \mathbf{e}_1 \pm i \sin \phi \mathbf{e}_2$, where “ \pm ” denotes the right- or left-handed elliptical light and ϕ determines its helicity. In particular, $\phi = \pm 45^\circ$ corresponds to circularly polarized light.

In our work, we consider both normal and oblique incidence of elliptically polarized light. At normal incidence, the light is irradiated vertically on the central region of the device along the y axis. In this case, the polarization vector, \mathbf{e} , is located in the x - z plane and forms an angle ϕ with respect to the z direction, as shown in Fig. 1(d). At oblique incidence, we consider three cases, in which the incidence plane is located in the x - y , x - z , and y - z planes. Specifically, at oblique incidence within the x - y plane, we can set \mathbf{e}_1 along the z axis, i.e.,

$$\mathbf{e}_1 = -\mathbf{k}, \quad \mathbf{e}_2 = \cos \alpha \mathbf{i} - \sin \alpha \mathbf{j}, \quad (2)$$

where \mathbf{i} , \mathbf{j} , and \mathbf{k} are unit vectors along the x , y , and z axes, respectively. Here, α is the incidence angle, formed by the transport direction of light with respect to the y axis. Therefore, by substituting Eq. (2) into $G_{1,2,3}^{>(<)(\text{ph})}$ in Eq. (1), we can rewrite the photocurrent at oblique incidence within the x - y plane as

$$J_L^{(\text{ph})} = \frac{ie}{h} \int \text{Tr} \left\{ \Gamma_L \left[G_4^{<(\text{ph})} + f_L \left(G_4^{>(\text{ph})} - G_4^{<(\text{ph})} \right) \right] \right\} dE, \quad (3)$$

where

$$\begin{aligned} G_4^{>(<)(\text{ph})} = & C_0 \cos^2 \alpha \sin^2 \phi \left(G_0^r p_x G_0^{>(<)} p_x^\dagger G_0^a \right) \\ & + C_0 \sin^2 \alpha \sin^2 \phi \left(G_0^r p_y G_0^{>(<)} p_y^\dagger G_0^a \right) \\ & - \frac{C_0}{2} \sin(2\alpha) \sin^2 \phi \left(G_0^r p_x G_0^{>(<)} p_y^\dagger G_0^a \right. \\ & \left. + G_0^r p_y G_0^{>(<)} p_x^\dagger G_0^a \right) \\ & + i \frac{C_0}{2} \cos \alpha \sin(2\phi) \left(G_0^r p_z G_0^{>(<)} p_x^\dagger G_0^a \right. \\ & \left. - G_0^r p_x G_0^{>(<)} p_z^\dagger G_0^a \right) \\ & + i \frac{C_0}{2} \sin \alpha \sin(2\phi) \left(G_0^r p_y G_0^{>(<)} p_z^\dagger G_0^a \right. \\ & \left. - G_0^r p_z G_0^{>(<)} p_y^\dagger G_0^a \right) \\ & + C_0 \cos^2 \phi \left(G_0^r p_z G_0^{>(<)} p_z^\dagger G_0^a \right). \end{aligned} \quad (4)$$

Equation (4) describes the dependence of the PGE photocurrent on both the incidence angle, α , and on the polarization angle, ϕ (helicity), under the illumination of elliptically polarized light. Here, $C_0 = (e/m_0)^2 \frac{\hbar \sqrt{\mu_r \epsilon_r}}{2N\omega \epsilon c} I_\omega$, where e and m_0 are the electronic charge and bare electron mass, respectively; I_ω is the photon flux, which is defined as the number of photons per unit time per unit area; ω and c are the frequency and speed of light, respectively; μ_r is the relative magnetic susceptibility; ϵ_r is the relative

dielectric constant; and ϵ is the dielectric constant. N is the number of photons. In the above expressions, $G_0^{r(a)}$ are the retarded (advanced) Green's functions without photons, $G_0^{>(<)}$ are the greater (lesser) Green's functions without photons. The photocurrent can be normalized as

$$I = J_L^{(\text{ph})} / eI_\omega, \quad (5)$$

which still has a dimension of area, i.e., a_0^2/photon , where a_0 is the Bohr radius.

The above method to calculate the PGE photocurrent is implemented in the quantum transport package NanoDCAL [59,62], and in the following, the photocurrent is calculated by NanoDCAL. In the electronic self-consistent calculations of the electrodes and center regions, the Brillouin zone is sampled using $10 \times 1 \times 100$ and $10 \times 1 \times 1$ grids of k points, respectively. In the photocurrent transport calculation, $16 \times 1 \times 1$ k points are used. All physical quantities are expanded using the double-zeta-polarized (DZP) atomic orbital basis, the exchange-correlation potential is treated with the PBE functional [53], and the atomic cores are defined by the standard norm-conserving nonlocal pseudopotentials.

III. RESULTS AND DISCUSSION

A. Electronic band structures of the InSe/In₂Se₃ FE HJs

Figures 2(a) and 2(b) show the electronic band structures of the two FE HJs, which are calculated with both the HSE (solid lines) and PBE (dashed lines) functionals. The InSe/In₂Se₃(\downarrow) and InSe/In₂Se₃(\uparrow) HJs have indirect band gaps of 0.98 and 1.19 eV (HSE), while the PBE band gaps are 0.47 and 0.52 eV, respectively. Besides, both the HJs have the type-II band alignment, as indicated in Figs. 2(c) and 2(d). Specifically, for the InSe/In₂Se₃(\downarrow) HJ, the electron charge at the valence-band maximum (VBM) is mainly contributed to by the InSe monolayer, while the conduction-band minimum (CBM) comes almost exclusively from the In₂Se₃ FE monolayer [Fig. 2(c)]. In contrast, if the FE polarization direction is reversed, i.e., for the InSe/In₂Se₃(\uparrow) HJ, the VBM comes mainly from FE In₂Se₃, while the CBM is contributed to by the InSe monolayer [Fig. 2(d)]. These results are in good agreement with previous first-principles calculations [48,49].

We then use the NEB method to calculate the kinetic pathway of the α -In₂Se₃ monolayer and the InSe/In₂Se₃ HJ from the initial state [In₂Se₃(\downarrow)] to the final state [In₂Se₃(\uparrow)], where the movement of the Se atom in the middle position of α -In₂Se₃ reflects the kinetic pathways. Figure 2(e) shows the kinetic pathway of the α -In₂Se₃ monolayer with an energy barrier of 1.05 eV, which is consistent with the previous result (1.02 eV) [63]. The kinetic pathway of the InSe/In₂Se₃ HJ is shown in Fig. 2(f). The energy barrier between the two HJs is 1.10 eV, which

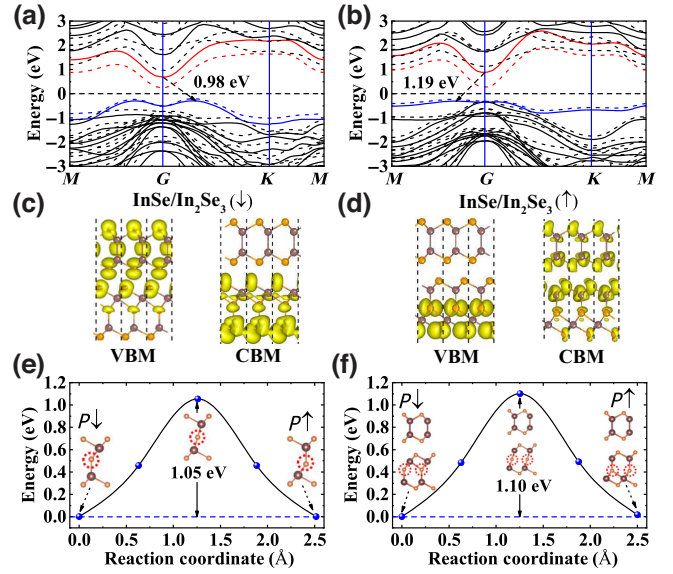


FIG. 2. (a),(b) Electronic band structures of the InSe/In₂Se₃(\downarrow) and InSe/In₂Se₃(\uparrow) HJs, respectively. (c),(d) Charge distributions of the VBM and CBM for the two HJs. (e) Kinetic pathways of the FE polarization-reversal processes for the α -In₂Se₃ monolayer and (f) InSe/In₂Se₃ HJs.

means that reversing the FE polarization of the InSe/In₂Se₃ HJ requires a larger external electrical field. Therefore, the two HJs have robust stability against the possible phase transitions between each other caused by external disturbance.

B. Photogalvanic effect of the InSe/In₂Se₃ FE HJs under the illumination of elliptically polarized light

The PGE can be generated when the central region is illuminated by elliptically polarized light due to the C_{3v} symmetry of the device, and the produced photocurrent flows out of the center region along the armchair (z) direction through the electrodes. The photocurrent is calculated with the PBE functional, as the HSE method is much more time consuming for such a large device. The PBE band gaps of the InSe/In₂Se₃(\downarrow) and InSe/In₂Se₃(\uparrow) FE HJs are 0.47 and 0.52 eV, respectively. Therefore, we consider the photon energies from 0.7 to 3.2 eV, which are above the band gap and cover the whole visible range, and then calculate the photocurrent at intervals of 0.1 eV for both normal and oblique incidence.

We first investigate the variation of photocurrent with light helicity (ϕ) for the InSe/In₂Se₃(\downarrow) FE HJ, as shown in Fig. 3. Our calculations show that, at normal incidence along the y axis, the photocurrent (I) has a cosine dependence on the light helicity, ϕ , in the form $I = A \cos(2\phi) + I_0$ for all photon energies. Figure 3(a) shows the photocurrents for photon energies of 1.3, 2.0, 2.4, and 3.0 eV as examples. It shows that the photocurrent for 2.0 eV can be well fitted with a function, $I = 0.018 \cos(2\phi) - 0.009$.

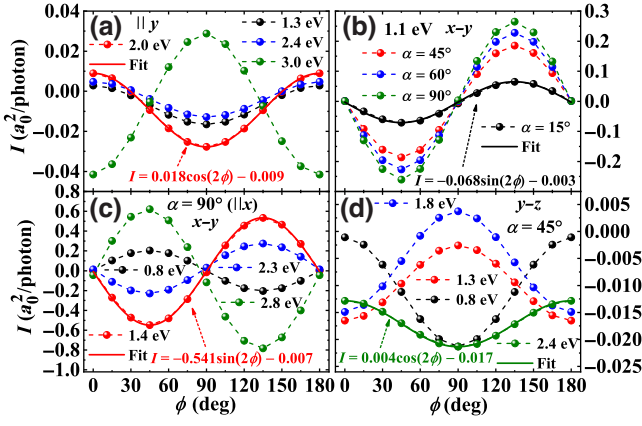


FIG. 3. Variation of photocurrent with light helicity, ϕ , for the InSe/In₂Se₃(\downarrow) HJ. (a) Photocurrent for different photon energies at normal incidence along the y axis. (b) Photocurrent at oblique incidence within the x - y plane for a photon energy of 1.1 eV with different incidence angles, α . (c),(d) Photocurrents at oblique incidence within the x - y and y - z planes, respectively, for different photon energies.

This cosine behavior of the photocurrent is a typical feature of the LPGE due to C_{3v} symmetry. At oblique incidence within the x - y plane, both the LPGE and CPGE can be generated. We find that the dependence of the photocurrent on the helicity, ϕ , changes to a sine function of $I = B \sin(2\phi) + I_0$, indicating that the CPGE plays a dominant role (see Sec. III C). For example, Fig. 3(b) shows the photocurrents as a function of ϕ at different incidence angles, α , for a photon energy of 1.1 eV. It can be seen that the photocurrent at $\alpha = 15^\circ$ is well fitted with the function $I = -0.068 \sin(2\phi) - 0.003$. In particular, we calculate the photocurrents at $\alpha = 90^\circ$ (parallel to the x axis) for photon energies of 0.8, 1.4, 2.3, and 2.8 eV. These photocurrents all follow $\sin(2\phi)$ behavior, as shown in Fig. 3(c). However, at oblique incidence within the y - z plane, the photocurrent displays a $\cos(2\phi)$ relationship with the light helicity, suggesting that the LPGE is the dominant mechanism. Examples are shown in Fig. 3(d) for photon energies of 0.8, 1.3, 1.8, and 2.4 eV at $\alpha = 45^\circ$.

We next investigate the photocurrent as a function of different incidence angles, α , at oblique incidence within the x - y and y - z planes. Within the x - y plane, the photocurrent has the form $I = C \sin \alpha + I_0$. As an example, in Fig. 4(a), we present the photocurrents as a function of α for photon energies of 0.8, 1.5, 2.3, and 2.8 eV with $\phi = 45^\circ$. It can be seen that the photocurrent for 1.5 eV can be perfectly fitted by the function $I = -0.528 \sin \alpha - 0.001$. At oblique incidence within the y - z plane, we find that, for most of the photon energies, e.g., 0.8, 0.9, and 1.0 eV, the photocurrent has the $\sin(2\alpha)$ form, while, for a few of the photon energies, e.g., 2.4 eV, the photocurrent has the $\cos(2\alpha)$ form, as shown in Fig. 4(b) at $\phi = 90^\circ$.

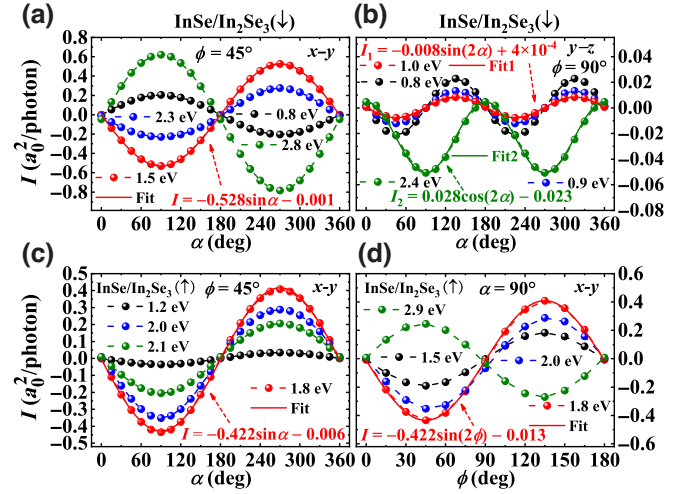


FIG. 4. Photocurrent as a function of incidence angle, α , at oblique incidence within the (a) x - y and (b) y - z planes for different photon energies with $\phi = 45^\circ$ and 90° , respectively, for the InSe/In₂Se₃(\downarrow) HJ. (c),(d) Dependence of the photocurrent on α and ϕ at oblique incidence within the x - y plane for the InSe/In₂Se₃(\uparrow) HJ.

For the InSe/In₂Se₃(\uparrow) HJ, the qualitative behaviors of the photocurrents are similar to those in the InSe/In₂Se₃(\downarrow) HJ, since both the HJs have the same C_{3v} symmetry. For example, Figs. 4(c) and 4(d) show that the photocurrents also have a sine dependence on both α and ϕ ; this is similar to the InSe/In₂Se₃(\downarrow) HJ [see Figs. 4(a) and 3(c)].

C. Discussion

Having investigated the dependence of the photocurrent on the light helicity, ϕ , and on the incidence angle, α , at normal and oblique incidence for both the InSe/In₂Se₃ FE HJs, we next clarify the contribution of the LPGE and CPGE to the photocurrent.

The dependence of the LPGE and CPGE photocurrents on ϕ and α is exclusively determined by material symmetry, according to phenomenological theory [1]. Therefore, owing to C_{3v} symmetry, the LPGE photocurrent in the InSe/In₂Se₃ FE HJs can be written as [40,41]

$$\begin{aligned} J_x^{\text{LPGE}} &= \chi \{E_x E_y^*\} + \chi' \{E_x E_z^*\}, \\ J_z^{\text{LPGE}} &= \chi \{E_z E_y^*\} + \chi' (|E_x|^2 - |E_z|^2), \end{aligned} \quad (6)$$

where $\{E_\mu E_\nu^*\} = E_\mu E_\nu^* + E_\nu E_\mu^*$, λ , and μ denote the three Cartesian components (x , y , and z). χ and χ' are third-order tensors that are dependent on the photon energy and material symmetry, and $E_{x,y,z}$ denotes the three components of the light electrical field. Notably, the dimension of the photocurrent, $J_{x,z}$, in Eq. (6) is different from that of I in Eq. (5), which is actually the photoresponse.

For a material with C_{3v} symmetry, tensors χ and χ' are linearly independent and have the following components,

respectively,

$$\chi \equiv \chi_{xy} = \chi_{zy}, \quad \chi' \equiv \chi_{xz} = \chi_{zx} = -\chi_{zz}, \quad (7)$$

where only χ_{zy} , χ_{zx} , and χ_{zz} contribute to J_z , according to Eq. (6). In our model, the HJs are located in the x - z plane, and the photocurrent, I , flows along the z axis (arm-chair direction), corresponding to J_z in Eq. (6). At normal incidence (parallel to the y axis),

$$E_x = E_0 \sin \phi, E_z = iE_0 \cos \phi, E_y = 0.$$

Therefore, only χ' , i.e., χ_{zx} and χ_{zz} , contribute to the photocurrent, while the contribution from χ_{zy} is zero, since $E_y = 0$. However, at oblique incidence, $E_y \neq 0$, all three components, χ_{zy} , χ_{zx} , and χ_{zz} , contribute to the LPGE photocurrent, according to Eq. (6).

In addition to the LPGE, the CPGE can be induced at oblique incidence of elliptically polarized light. This effect is expressed phenomenologically as

$$J_\lambda^{\text{CPGE}} = \sum_\mu \gamma_{\lambda\mu} i(\mathbf{E} \times \mathbf{E}^*)_\mu, \quad (8)$$

where $\gamma_{\lambda\mu}$ is a second-order pseudotensor. For C_{3v} symmetry, $\gamma_{\lambda\mu}$ has two components, $\gamma_{xz} = -\gamma_{zx} \equiv \gamma$, while only γ_{zx} contributes to the CPGE photocurrent, J_z , flowing along the z direction.

At oblique incidence within the x - y plane, the three components of the electrical field on the x , y , and z axes can be written as

$$E_x = E_0 \sin \phi \cos \alpha, E_y = E_0 \sin \phi \sin \alpha, E_z = E_0 \cos \phi. \quad (9)$$

Substituting Eq. (9) into Eqs. (6) and (8), we obtain the photocurrent, J_z , at oblique incidence within the x - y plane:

$$J_z^{x-y} = -\gamma_{zx} E_0^2 \sin(2\phi) \sin \alpha + \chi_{zx} E_0^2 \sin^2 \phi \cos^2 \alpha + \chi_{zz} E_0^2 \cos^2 \phi, \quad (10)$$

Similarly, at oblique incidence within the x - z plane, we obtain the photocurrent:

$$J_z^{x-z} = \gamma_{zx} E_0^2 \sin(2\phi) \sin \alpha + \chi_{zx} E_0^2 \sin^2 \phi \cos^2 \alpha + \chi_{zz} E_0^2 \sin^2 \phi \sin^2 \alpha, \quad (11)$$

where $\alpha = 0^\circ$ means the incidence is along the z direction. Equations (10) and (11) include the contributions from both the LPGE (χ') and the CPGE (γ). In addition, at oblique incidence within the y - z plane, we obtain the

photocurrent:

$$J_z^{y-z} = -\chi_{zy} \frac{E_0^2}{2} \sin^2 \phi \sin 2\alpha + \chi_{zx} E_0^2 \cos^2 \phi + \chi_{zz} E_0^2 \sin^2 \phi \cos^2 \alpha, \quad (12)$$

where only the LPGE contributes to the photocurrent from both χ (χ_{zy}) and χ' (χ_{zz} , χ_{zx}). Notably, there is still the CPGE photocurrent in the x direction at the incidence within the y - z plane due to γ_{xz} , according to Eq. (8).

Then by comparing Eq. (10) with Eq. (4), we can further identify χ_{zz} and χ_{zx} for the LPGE and γ_{zx} for the CPGE based on our calculated photocurrents. Specifically, in Eq. (4), by setting (i) $\phi, \alpha = 0^\circ$, we obtain $I_1 = D\chi_{zz}$; (ii) for $\phi = 90^\circ, \alpha = 0^\circ$, we get $I_2 = D\chi_{zx}$; and (iii) for $\phi = 45^\circ, \alpha = 90^\circ$, we get $I_3 = D(\frac{1}{2}\chi_{zz} - \gamma_{zx})$, where D is a coefficient. Therefore, we can compare the contributions of the LPGE and CPGE in terms of $I_{1,2,3}$. For example, $|\gamma/\chi_{zx}| = |(I_1/2 - I_3)/I_2|$, where $\gamma \equiv \gamma_{zx}$. Similarly, we can also obtain χ , i.e., χ_{zy} , based on the calculated photocurrent at oblique incidence within the y - z plane by comparing it with Eq. (12). Therefore, we can compare the contributions from all the individual components of the LPGE and CPGE, as shown in Fig. 5. It is worth noting that the photocurrent in Eq. (3) is a general form of the PGE photocurrent, which is suitable for any symmetry. This means that, with a specific symmetry, only some of the terms on the right side of Eq. (4) appear, while other terms should vanish, in principle (negligible in magnitude). Here, for the InSe/In₂Se₃ HJs with C_{3v} symmetry, this means that at oblique incidence within the x - y plane only the first, fifth, and last terms in Eq. (4) occur; these correspond to χ_{zx} , γ_{zx} , and χ_{zz} , respectively. Other terms, e.g., χ_{zy} , are indeed negligible in magnitude according to our calculation.

Figure 5(a) shows the ratios of $|\gamma/\chi_{zx}|$ and $|\gamma/\chi_{zz}|$. It can be seen that γ is much larger than χ' (χ_{zx} and χ_{zz}) for most of the photon energies, with the largest ratio of up to 10^3 . This means that, at oblique incidence within the x - y or x - z planes, the photocurrent is dominated by the CPGE, according to Eqs. (10) and (11). Correspondingly, the photocurrent has a $\sin \alpha$ dependence on the incidence angle, α , which comes from the first term in Eqs. (10) and (11), as shown in Fig. 4(a). We also find that, only at 2.1 eV, γ is less than χ_{zx} and χ_{zz} , and correspondingly, the photocurrent has comparable contributions from both $\sin \alpha$ and $\cos(2\alpha)$, according to Eq. (10), as shown in Fig. 5(b). In addition, we note that $|\gamma/\chi_{zz}|$ should be equal to $|\gamma/\chi_{zx}|$, since $\chi_{zx} = -\chi_{zz}$, according to Eq. (7), for C_{3v} symmetry. However, in our first-principles simulations, the device model is fully relaxed in the atomic configuration, which breaks exact C_{3v} symmetry, and therefore, leads to the difference between χ_{zx} and $-\chi_{zz}$. Nevertheless, $|\gamma/\chi_{zz}|$ and $|\gamma/\chi_{zx}|$ still have similar qualitative trends and little difference in magnitude for most of the photon energies.

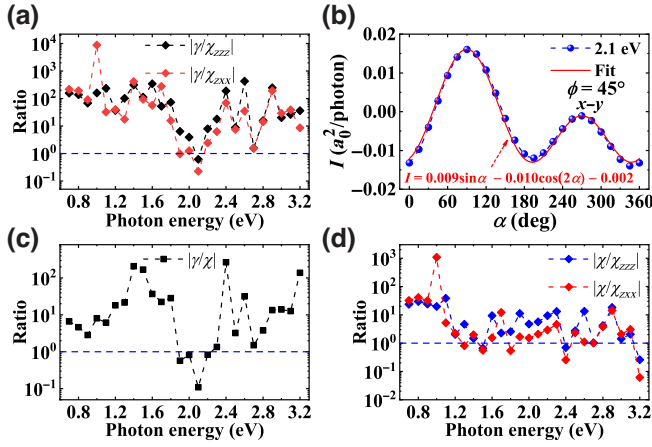


FIG. 5. Comparisons between the LPGE and CPGE for the InSe/In₂Se₃(↓) FE HJ. (a) Ratio between γ and χ' at different photon energies. (b) The calculated and the fitted photocurrent at 2.1 eV at oblique incidence within the x - y plane. (c) Comparison between γ and χ , and (d) between χ and χ' .

Figure 5(c) shows that γ is also evidently larger than χ (χ_{zzy}) for most of the photon energies, except for 1.9, 2.0, 2.1, and 2.2 eV. Additionally, Fig. 5(d) shows that, for most of the photon energies, χ (χ_{zzy}) is greater than χ' . This means that, at oblique incidence within the y - z plane, the photocurrent is mainly contributed to by the first term in Eq. (12), leading to $\sin(2\alpha)$ behavior, as shown in Fig. 4(b). For three photon energies of 1.5, 2.4, and 3.2 eV, χ is less than χ' , and correspondingly, the photocurrent shows a $\cos(2\alpha)$ curve [see the green line in Fig. 4(b)], which comes from the last term in Eq. (12).

The above analysis shows that the CPGE can be much larger than the LPGE for most of photon energies from 0.7 to 3.2 eV for the InSe/In₂Se₃(↓) FE HJ. It is well known that the PGE photocurrent is proportional to both the optical absorption and asymmetric parameter of photoexcitation. Notably, the optical absorption coefficient is the same for the LPGE and CPGE, as both are induced under illumination from the same elliptically polarized light. Therefore, the larger CPGE photocurrent is due to its larger photoexcitation asymmetry, compared to that of the LPGE.

We next investigate the maximum photocurrent (I_{\max}) at different incidence angles, α . At oblique incidence within the x - y and x - z planes, the maximum photocurrent appears at $\alpha = 90^\circ$ or 270° [see Eqs. (10) and (11)], which corresponds to the incidence direction along the x axis. For oblique incidence within the y - z plane, I_{\max} can occur at $\alpha = 0^\circ, 45^\circ, 90^\circ$, or 135° . For comparison, we give I_{\max} in Fig. 6(a) for different photon energies at incidence along the x and y axes and within the y - z plane. It can be seen that I_{\max} at incidence along the x axis (black squares) is much larger than that at incidence along the y axis and within the y - z plane for most of the photon energies. To understand

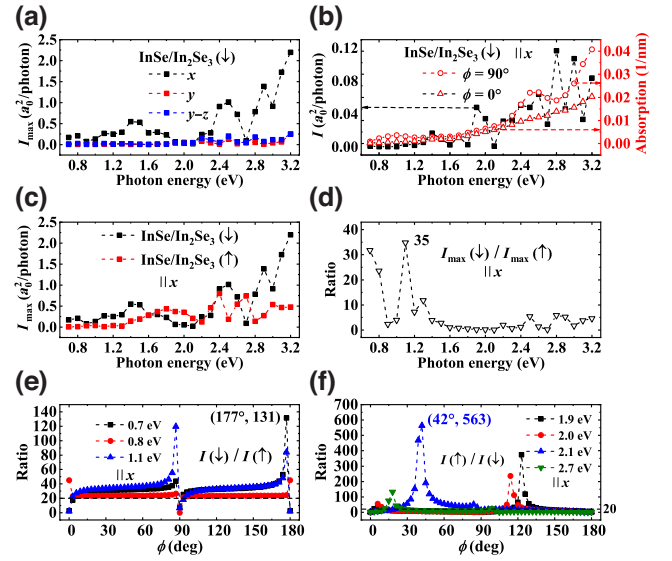


FIG. 6. (a) Photocurrent of the InSe/In₂Se₃(↓) HJ as a function of photon energy at incidence along the x and y axes and at oblique incidence within the y - z plane. (b) Photocurrent at incidence along the x direction, and the optical absorption at polarization angles of $\phi = 90^\circ$ and 0° . (c) Variation of I_{\max} with photon energy for the InSe/In₂Se₃(↓) and InSe/In₂Se₃(↑) HJs at incidence along the x axis, and (d) the ratio of I_{\max} between the two HJs. (e),(f) Ratio of the photocurrent between the InSe/In₂Se₃(↓) and InSe/In₂Se₃(↑) HJs at different light helicities, ϕ .

the variation of the photocurrent with photon energy, in Fig. 6(b), we show the photocurrent spectra for light incident along the x direction (black squares) and the optical absorption coefficient (red circles) at polarization angles of $\phi = 90^\circ$ and 0° . We find that the overall trend of the PGE photocurrent agrees with that of the optical absorption. The mismatch between the photocurrent and absorption should be ascribed to different excitation asymmetry [1], which depends on the valance and conduction bands, where the electron transition takes place, and hence, varies with the photon energy.

We then examine the influence of FE polarization reversal on I_{\max} at incidence along the x axis for different photon energies. Figure 6(c) gives I_{\max} along the x axis for the InSe/In₂Se₃(↓) and InSe/In₂Se₃(↑) HJs. It shows that, at lower photon energies from 0.7 to 1.5 eV, and higher photon energies from 2.8 to 3.2 eV, the photocurrent of the InSe/In₂Se₃(↓) HJ is obviously larger than that of the InSe/In₂Se₃(↑) HJ. The largest switching ratio of 35 is achieved at 1.1 eV [see Fig. 6(d)]. In the lower-photon-energy range, from 0.7 to 1.5 eV, the electron transitions are mainly from the top valence band to the lower conduction bands close to the Fermi level. As already mentioned, the CBM is mainly contributed to by In₂Se₃ for the InSe/In₂Se₃(↓) HJ, while the CBM for the InSe/In₂Se₃(↑) HJ is mainly from the InSe monolayer. Therefore, the

PGE photocurrent (electrons) mostly flows in In_2Se_3 for the $\text{InSe}/\text{In}_2\text{Se}_3(\downarrow)$ HJ, while the photocurrent flows in InSe for the $\text{InSe}/\text{In}_2\text{Se}_3(\uparrow)$ HJ. Notably, In_2Se_3 has C_{3v} symmetry, whereas InSe has higher symmetry, D_{3h} , which means that the PGE photocurrent in In_2Se_3 should be larger than that in InSe , as the PGE photocurrent is proportional to the asymmetry of the material. A lower symmetry tends to induce a larger PGE photocurrent. For higher photon energies (> 1.6 eV), the conduction bands and valence bands have mutual contributions from both InSe and In_2Se_3 . The large switching ratio should be ascribed to electron transitions between the valence and conduction bands, which have different asymmetry, leading to different photocurrents for the two HJs.

Furthermore, we compare the photocurrents of the two HJs by calculating the switching ratios of $I(\uparrow)/I(\downarrow)$ and $I(\downarrow)/I(\uparrow)$ at different helicity, ϕ . Here, $I(\downarrow)$ and $I(\uparrow)$ denote the photocurrents at helicity ϕ for the $\text{InSe}/\text{In}_2\text{Se}_3(\downarrow)$ and $\text{InSe}/\text{In}_2\text{Se}_3(\uparrow)$ HJs, respectively. Figure 6(e) shows the switching ratio of $I(\downarrow)/I(\uparrow)$ for photon energies of 0.7, 0.8, and 1.1 eV, and Fig. 6(f) shows the switching ratio of $I(\uparrow)/I(\downarrow)$ for photon energies of 1.9, 2.0, 2.1, and 2.7 eV. We observe that, over a wide helicity range, the switching ratio is greater than 20 (an acceptable value for commercial applications [28]). The largest switching ratio reaches 563 at $\phi = 42^\circ$ for a photon energy of 2.1 eV, as shown in Fig. 6(f). These results suggest that a large switching ratio can be achieved by tuning the photon energy and light helicity. In experiments, switching of the ferroelectric polarization of $\alpha\text{-In}_2\text{Se}_3$ can be realized by applying an electrical field and reversing its direction [64].

We next examine the influence of FE switching on the direction of the photocurrent for incidence along the x direction. We find that, for 12 photon energies, e.g., 1.8 eV, the photocurrent does not change sign when the FE polarization of In_2Se_3 is reversed from downward to upward [Fig. 7(a)], while, for 14 photon energies, e.g., 2.3 eV, the photocurrent changes its sign, as shown in Fig. 7(b). Notably, both FE polarization and heterostructure stacking along the y direction break the original mirror symmetry with respect to the x - z plane in D_{3h} of the InSe monolayer, which leads to the PGE. These results indicate that FE polarization in In_2Se_3 and heterostructure stacking along the y direction play almost equal roles in determining the behavior of the PGE.

Finally, we investigate the light-polarization (helicity) sensitivity of the photocurrent. At incidence along the y and z axes, the photocurrent takes a $\cos(2\phi)$ form, as shown in Figs. 3(a) and 3(d). Then, to evaluate the polarization sensitivity, we can define the extinction ratio as $R = |I_{\max}/I_{\min}|$ [65,66], where I_{\max} and I_{\min} are achieved at $\phi = 90^\circ$ or $\phi = 0^\circ$, respectively. Figures 7(c) and 7(d) show the extinction ratios at incidence along the y and z axes for both HJs, respectively. The largest extinction ratio is 410 (1.9 eV) at incidence along the y axis for the

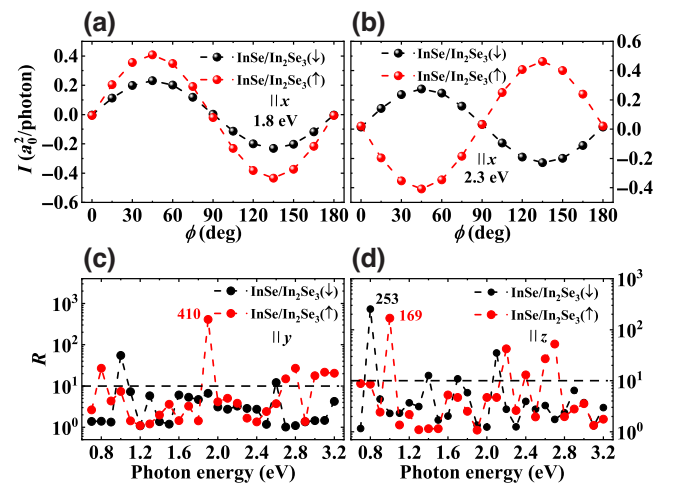


FIG. 7. (a),(b) Photocurrents at 1.8 and 2.3 eV for the $\text{InSe}/\text{In}_2\text{Se}_3$ HJs, respectively. (c),(d) Extinction ratios of the $\text{InSe}/\text{In}_2\text{Se}_3(\downarrow)$ and $\text{InSe}/\text{In}_2\text{Se}_3(\uparrow)$ HJs at incidence along the y and z axes, respectively.

$\text{InSe}/\text{In}_2\text{Se}_3(\uparrow)$ HJ [Fig. 7(c)], while at incidence along the z axis the largest extinction ratio is 253 (0.8 eV) for the $\text{InSe}/\text{In}_2\text{Se}_3(\downarrow)$ HJ [Fig. 7(d)]. Additionally, for a number of photon energies, the extinction ratio is greater than 10 (see those above the black dashed lines). Many recent experiments demonstrated various 2D photodetectors with light-polarization sensitivity [67–75]. The largest reported extinction ratio is 288 at 1450 nm, which is obtained with a 2D black-phosphorous photodetector [35]. However, only recently have PGE-driven polarization-sensitive photodetectors been realized in experiments by using 2D FE perovskite materials [23–26]; the largest extinction ratio is 15. Here, our proposed $\text{InSe}/\text{In}_2\text{Se}_3(\uparrow)$ FE HJs show large extinction ratios, which are also tunable by FE polarization reversal. The large extinction ratio originates from the significant anisotropy in the optical absorption and electrical properties between the x , y , and z directions. In Fig. 6(b), we show the optical absorption of the $\text{InSe}/\text{In}_2\text{Se}_3(\downarrow)$ HJ for light polarization parallel to the x ($\phi = 0^\circ$) and y directions ($\phi = 90^\circ$). An evident difference in optical absorption between these two directions can be observed, which results in a large difference in the photoexcitation of electrons, and therefore, different photocurrents at $\phi = 90^\circ$ and $\phi = 0^\circ$.

It is worth noting that, for these two incidence directions, only the LPGE is induced, according to Eqs. (10) and (11), at $\alpha = 0^\circ$. This means that the extinction ratios in Figs. 7(c) and 7(d) are, in fact, for linearly polarized light, and therefore, cannot be used to distinguish linearly polarized light from elliptically polarized light. However, we can identify them by the behavior of the photocurrent. For example, for elliptically polarized light with the incidence in the x - y plane, the CPGE is dominant, and the photocurrent has a $\sin(2\phi)$ dependence, as shown in Figs. 3(b)

and 3(c). In contrast, for linearly polarized light, only the LPGE is generated and the photocurrent shows a $\cos(2\phi)$ dependence, according to the last two terms in Eq. (10). Such different behaviors of the photocurrents on the light helicity (polarization) can be used to distinguish linearly polarized light from elliptically polarized light. The potential application of the (light) polarization sensitivity of the CPGE and LPGE was recently explored [76]. Briefly speaking, based on the polarization (helicity) dependence of the PGE photocurrent (photovoltage), the Stokes vector can be obtained for polarization imaging; this is widely applied in military and civil applications, including mine detection, anticamouflage recognition, medical diagnosis, and astronomy.

In our device model, we do not consider metallic electrodes, since we focus on the intrinsic PGE generated in the semiconducting InSe/In₂Se₃ HJ. The external influence of the metallic electrodes is therefore not considered, although experiments have shown that the metallic electrodes have a critical impact on the PGE [77–79]. In addition, the proposed InSe/In₂Se₃ HJ has not been fabricated in experiments. We note that the vertical heterojunction composed of monolayer WSe₂/In₂Se₃ has been fabricated in experiments; this has a type-II band alignment [80]. Additionally, photodetectors based on α -In₂Se₃/WSe₂ [81], α -In₂Se₃/MoS₂ [82], and α -In₂Se₃/black phosphorous [83] vertical heterojunctions have also been fabricated. These experiments make it promising to fabricate the InSe/In₂Se₃ heterojunction in the future.

We note that there are limitations in our photocurrent calculations when using the nonequilibrium Green's functional formalism within a ballistic transport regime. Kinetic processes, such as electron-phonon scattering and recombination, are not considered. However, ballistic transport can take place at a low enough temperature with a finite channel length that is shorter than the free mean path of electrons, and therefore, phonon scattering can be severely suppressed. Moreover, experiments have shown that the robust PGE photocurrent in ferroelectric tetrathiafulvalene-*p*-chloranil can be generated over a wide photon-energy range (0.6 to 2.5 eV) that is much greater than the material's band gap (0.6 eV) [84], indicating that the kinetic processes of scattering (relaxation) and recombination do not play the main role in producing the PGE photocurrent.

IV. CONCLUSIONS

We investigate both the LPGE and CPGE of 2D InSe/In₂Se₃ FE HJs induced by elliptically polarized light by using quantum transport simulations. Both the LPGE and CPGE can be generated over the whole visible range for both the InSe/In₂Se₃(↓) and InSe/In₂Se₃(↑) HJs, owing to the noncentrosymmetric C_{3v} symmetry. The

dependence of the photocurrent on the incident angle, α , and on the light helicity, ϕ , is revealed. The CPGE can be much larger than the LPGE for most photon energies in the range of 0.7 to 3.2 eV, with the largest ratio of up to 10^3 . The photocurrent can be tuned by FE polarization switching, leading to a large switching ratio of up to 563. Moreover, the InSe/In₂Se₃ HJs show a considerable light-polarization sensitivity, with a large extinction ratio of 410. These results suggest that the CPGE in the 2D FE materials is also promising in various fields, such as nonvolatile memory, self-powered photodetection, and solar cells, as compared to the LPGE.

ACKNOWLEDGMENTS

This work is supported by the National Natural Science Foundation of China under Grant No. 51871156.

-
- [1] V. I. Belinicher and B. I. Sturman, The photogalvanic effect in media lacking a center of symmetry, *Sov. Phys. Usp.* **23**, 199 (1980).
 - [2] X. Tao, P. Jiang, H. Hao, X. Zheng, L. Zhang, and Z. Zeng, Pure spin current generation via photogalvanic effect with spatial inversion symmetry, *Phys. Rev. B* **102**, 081402(R) (2020).
 - [3] R. Fei, W. Song, L. P. Nazzaro, and L. Yang, *PT*-Symmetry-Enabled Spin Circular Photogalvanic Effect in Antiferromagnetic Insulators, *Phys. Rev. Lett.* **127**, 207402 (2021).
 - [4] H. Ishizuka and M. Sato, Large Photogalvanic Spin Current by Magnetic Resonance in Bilayer Cr Trihalides, *Phys. Rev. Lett.* **129**, 107201 (2022).
 - [5] A. Abdelsamie, L. You, L. Wang, S. Li, M. Gu, and J. Wang, Crossover between Bulk and Interface Photovoltaic Mechanisms in a Ferroelectric Vertical Heterostructure, *Phys. Rev. Appl.* **17**, 024047 (2022).
 - [6] L. Li, P. Yuan, T. Liu, Z. Ma, C. Xia, and X. Li, Self-Powered Broadband Photodetector Based on a Monolayer InSe *p-i-n* Homojunction, *Phys. Rev. Appl.* **19**, 014039 (2023).
 - [7] A. M. Burger, L. Gao, R. Agarwal, A. Aprelev, J. E. Spanier, A. M. Rappe, and V. M. Fridkin, Shift photovoltaic current and magnetically induced bulk photocurrent in piezoelectric sillenite crystals, *Phys. Rev. B* **102**, 081113(R) (2020).
 - [8] W. Kraut and R. von Baltz, Anomalous bulk photovoltaic effect in ferroelectrics: A quadratic response theory, *Phys. Rev. B* **19**, 1548 (1979).
 - [9] R. von Baltz and W. Kraut, Theory of the bulk photovoltaic effect in pure crystals, *Phys. Rev. B* **23**, 5590 (1981).
 - [10] V. I. Belinicher, E. L. Ivchenko, and B. I. Sturman, Kinetic theory of the displacement photovoltaic effect in piezoelectrics, *Sov. Phys.* **56**, 359 (1982).
 - [11] V. I. Belinicher and B. I. Sturman, The relation between shift and ballistic currents in the theory of photogalvanic effect, *Ferroelectrics* **83**, 29 (1988).
 - [12] B. I. Sturman, Ballistic and shift currents in the bulk photovoltaic effect theory, *Phys.-Usp.* **63**, 407 (2020).

- [13] R. P. Tiwari, B. Birajdar, and R. K. Ghosh, First-principles calculation of shift current bulk photovoltaic effect in two-dimensional α -In₂Se₃, *Phys. Rev. B* **101**, 235448 (2020).
- [14] F. M. Xu, H. J. Su, Z. R. Gong, Y. D. Wei, H. Jin, and H. Guo, Controllable ferroelectricity and bulk photovoltaic effect in elemental group-V monolayers through strain engineering, *Phys. Rev. B* **106**, 195418 (2022).
- [15] V. M. Fridkin, Bulk photovoltaic effect in noncentrosymmetric crystals, *Crystallogr. Rep.* **46**, 654 (2001).
- [16] Y. J. Zhang, R. Taniguchi, S. Masubuchi, R. Moriya, K. Watanabe, T. Taniguchi, T. Sasagawa, and T. Machida, Switchable out-of-plane shift current in ferroelectric two-dimensional material CuInP₂S₆, *Appl. Phys. Lett.* **120**, 013103 (2022).
- [17] A. M. Glass, D. von der Linde, and T. J. Negran, High-voltage bulk photovoltaic effect and the photorefractive process in LiNbO₃, *Appl. Phys. Lett.* **25**, 233 (1974).
- [18] J. E. Spanier, V. M. Fridkin, A. M. Rappe, A. R. Akbashev, A. Polemi, Y. B. Q. Z. Q. G, S. M. Young, C. J. Hawley, D. Imbrenda, G. Xiao, A. L. Bennett-Jackson, and C. L. Johnson, Power conversion efficiency exceeding the Shockley-Queisser limit in a ferroelectric insulator, *Nat. Photonics* **10**, 611 (2016).
- [19] A. Pérez-Tomás, E. Chikoidze, Y. Dumont, M. R. Jennings, S. O. Russell, P. Vales-Castro, G. Catalan, M. Lira-Cantú, C. Ton-That, F. H. Teherani, V. E. Sandana, P. Bove, and D. J. Rogers, Giant bulk photovoltaic effect in solar cell architectures with ultra-wide bandgap Ga₂O₃ transparent conducting electrodes, *Mater. Today Energy* **14**, 100350 (2019).
- [20] H. M. Wei, M. X. Wang, Y. Q. Wu, and B. Q. Cao, Effect of substrate on domain structure and bulk photovoltaic property in epitaxial BiFeO₃ films, *Physica B* **650**, 414524 (2023).
- [21] S. Pal, S. Muthukrishnan, B. Sadhukhan, S. N. V. D. Murali, and P. Murugavel, Bulk photovoltaic effect in BaTiO₃-based ferroelectric oxides: An experimental and theoretical study, *J. Appl. Phys.* **129**, 084106 (2021).
- [22] S. G. Han, M. F. Li, Y. Liu, W. Q. Guo, M. C. Hong, Z. H. Sun, and J. H. Luo, Tailoring of a visible-light-absorbing biaxial ferroelectric towards broadband self-driven photodetection, *Nat. Commun.* **12**, 284 (2021).
- [23] H. Ye, Y. Peng, X. Y. Shang, L. N. Li, Y. P. Yao, X. Y. Zhang, T. T. Zhu, X. T. Liu, X. Y. Chen, and J. H. Luo, Self-powered visible-infrared polarization photodetection driven by ferroelectric photovoltaic effect in a Dion-Jacobson hybrid perovskite, *Adv. Funct. Mater.* **32**, 2200223 (2022).
- [24] Y. Peng, X. T. Liu, Z. H. Sun, C. M. Ji, L. N. Li, Z. Y. Wu, S. S. Wang, Y. P. Yao, M. C. Hong, and J. H. Luo, Exploiting the bulk photovoltaic effect in a 2D trilayered hybrid ferroelectric for highly sensitive polarized light detection, *Angew. Chem. Int. Ed.* **59**, 3933 (2020).
- [25] C. M. Ji, D. Dey, Y. Peng, X. T. Liu, L. N. Li, and J. H. Luo, Ferroelectricity-driven self-powered ultraviolet photodetection with strong polarization sensitivity in a two-dimensional halide hybrid perovskite, *Angew. Chem. Int. Ed.* **59**, 18933 (2020).
- [26] L. Lu, W. Weng, Y. Ma, Y. Liu, S. G. Han, X. T. Liu, H. J. Xu, W. X. Lin, Z. H. Sun, and J. H. Luo, Anisotropy in a 2D perovskite ferroelectric drives self-powered polarization-sensitive photoresponse for ultraviolet solar-blind polarized-light detection, *Angew. Chem. Int. Ed.* **61**, 202205030 (2022).
- [27] Y. P. Yao, Y. Peng, L. N. Li, X. Y. Zhang, X. T. Liu, M. C. Hong, and J. H. Luo, Exploring a fatigue-free layered hybrid perovskite ferroelectric for photovoltaic non-volatile memories, *Angew. Chem. Int. Ed.* **60**, 10598 (2021).
- [28] A. Lipatov, P. Sharma, A. Gruverman, and A. Sinitskii, Optoelectrical molybdenum disulfide (MoS₂)–ferroelectric memories, *ACS Nano* **9**, 8089 (2015).
- [29] J. Wang, Y. Y. Huang, Z. Lei, Y. Y. Xi, W. Y. Du, X. Q. Cao, Y. Q. Ge, L. P. Zhu, Y. X. Zhou, and X. L. Xu, Tunable polarized terahertz wave generation induced by spontaneous polarization-dependent ultrafast shift current from vertically grown ferroelectric SnS, *Phys. Rev. B* **106**, 235308 (2022).
- [30] M. N. Kamalasanan, S. Chandra, P. C. Joshi, and A. Mansingh, Structural and optical properties of sol-gel-processed BaTiO₃ ferroelectric thin films, *Appl. Phys. Lett.* **59**, 3547 (1991).
- [31] F. G. Zheng, Y. Xin, W. Huang, J. X. Zhang, X. F. Wang, M. R. Shen, W. Dong, L. Fang, Y. B. Bai, X. Q. Shen, and J. H. Hao, Above 1% efficiency of a ferroelectric solar cell based on the Pb(Zr, Ti)O₃ film, *J. Mater. Chem. A* **2**, 1363 (2014).
- [32] A. Bhatnagar, A. R. Chaudhuri, Y. H. Kim, D. Hesse, and M. Alexe, Role of domain walls in the abnormal photovoltaic effect in BiFeO₃, *Nat. Commun.* **4**, 2835 (2013).
- [33] J. F. Ihlefeld, N. J. Podraza, Z. K. Liu, R. C. Rai, X. Xu, T. Heeg, Y. B. Chen, J. Li, R. W. Collins, J. L. Musfeldt, X. Q. Pan, J. Schubert, R. Ramesh, and D. G. Schlom, Optical band gap of BiFeO₃ grown by molecular-beam epitaxy, *Appl. Phys. Lett.* **92**, 142908 (2008).
- [34] Y. Li, J. Fu, X. Y. Mao, C. Chen, H. Liu, M. Gong, and H. L. Zeng, Enhanced bulk photovoltaic effect in two-dimensional ferroelectric CuInP₂S₆, *Nat. Commun.* **12**, 5896 (2021).
- [35] S. Wu, Y. Chen, X. Wang, H. Jiao, Q. Zhao, X. Huang, X. Tai, Y. Zhou, H. Chen, X. Wang, S. Huang, H. Yan, T. Lin, H. Shen, W. Hu, X. Meng, J. Chu, and J. Wang, Ultra-sensitive polarization-resolved black phosphorus homojunction photodetector defined by ferroelectric domains, *Nat. Commun.* **13**, 3198 (2022).
- [36] T. Akamatsu, T. Ideue, L. Zhou, Y. Dong, S. Kitamura, M. Yoshii, D. Y. Yang, M. Onga, Y. Nakagawa, K. Watanabe, T. Taniguchi, J. Lauritzen, J. W. Huang, Z. L. Ye, T. Morimoto, H. T. Yuan, and Y. Iwasa, A van der Waals interface that creates in-plane polarization and a spontaneous photovoltaic effect, *Science* **372**, 68 (2021).
- [37] W. Ji, K. Yao, and Y. C. Liang, Evidence of bulk photovoltaic effect and large tensor coefficient in ferroelectric BiFeO₃ thin films, *Phys. Rev. B* **84**, 094115 (2011).
- [38] B. Luo, X. N. Ma, J. J. Liu, W. Wu, X. Yu, S. B. Hu, H. Gao, F. H. Jia, and W. Ren, Enhanced photogalvanic effect in a 2D ferroelectric ZrI₂ by interlayer sliding, *Physica E* **142**, 115297 (2022).
- [39] D. S. Knoche, M. Steimecke, Y. Yun, L. Mühlenbein, and A. Bhatnagar, Anomalous circular bulk photovoltaic

- effect in BiFeO₃ thin films with stripe-domain pattern, *Nat. Commun.* **12**, 282 (2021).
- [40] W. Weber, L. E. Golub, S. N. Danilov, J. Karch, C. Reitmaier, B. Wittmann, V. V. Bel'kov, E. L. Ivchenko, Z. D. Kvon, N. Q. Vinh, A. F. G. van der Meer, B. Murdin, and S. D. Ganichev, Quantum ratchet effects induced by terahertz radiation in GaN-based two-dimensional structures, *Phys. Rev. B* **77**, 245304 (2008).
- [41] B. Wittmann, L. E. Golub, S. N. Danilov, J. Karch, C. Reitmaier, Z. D. Kvon, N. Q. Vinh, A. F. G. van der Meer, B. Murdin, and S. D. Ganichev, Resonant circular photogalvanic effect in GaN/AlGaN heterojunctions, *Phys. Rev. B* **78**, 205435 (2008).
- [42] M. Soleimani and M. Pourfath, Ferroelectricity and phase transitions in In₂Se₃ van der Waals material, *Nanoscale* **12**, 22688 (2020).
- [43] W. J. Ding, J. B. Zhu, Z. Wang, Y. F. Gao, D. Xiao, Y. Gu, Z. Y. Zhang, and W. G. Zhu, Prediction of intrinsic two-dimensional ferroelectrics in In₂Se₃ and other III₂-VI₃ van der Waals materials, *Nat. Commun.* **8**, 14956 (2017).
- [44] Y. Zhou, D. Wu, Y. H. Zhu, Y. J. Cho, Q. He, X. Yang, K. Herrera, Z. D. Chu, Y. Han, M. C. Downer, H. L. Peng, and K. J. Lai, Out-of-plane piezoelectricity and ferroelectricity in layered α -In₂Se₃ nanoflakes, *Nano Lett.* **17**, 5508 (2017).
- [45] C. J. Cui, W. J. Hu, X. X. Yan, C. Addiego, W. P. Gao, Y. Wang, Z. Wang, L. Z. Li, Y. C. Cheng, P. Li, X. X. Zhang, H. N. Alshareef, T. Wu, W. G. Zhu, X. Q. Pan, and L. J. Li, Intercorrelated in-plane and out-of-plane ferroelectricity in ultrathin two-dimensional layered semiconductor In₂Se₃, *Nano Lett.* **18**, 1253 (2018).
- [46] S. Y. Wan, Y. Li, W. Li, X. Y. Mao, W. G. Zhu, and H. L. Zeng, Room-temperature ferroelectricity and a switchable diode effect in two-dimensional α -In₂Se₃ thin layers, *Nanoscale* **10**, 14885 (2018).
- [47] Y. Q. Yang, L. W. Zhang, J. Chen, X. H. Zheng, L. Zhang, L. T. Xiao, and S. T. Jia, An electrically switchable anti-ferroelectric bilayer In₂Se₃ based opto-spintronic device, *Nanoscale* **13**, 8555 (2021).
- [48] Y. N. Li, Y. Q. Xie, and Y. Wang, Strain control of two-dimensional ferroelectric In₂Se₃/InSe vertical heterojunction energy band, *Acta Phys. Sin.* **70**, 227701 (2021).
- [49] X. K. Duan, S. Y. Tang, and Z. Huang, Tuning the electronic properties of two dimensional InSe/In₂Se₃ heterostructure via ferroelectric polarization and strain, *Comput. Mater. Sci.* **200**, 110819 (2021).
- [50] For details of the DS-PAW first-principles plane-wave package, see <http://iresearch.net.cn/web/product-service?id=10>.
- [51] T. Hu, J. Zhou, and J. M. Dong, Strain induced new phase and indirect-direct band gap transition of monolayer InSe, *Phys. Chem. Chem. Phys.* **19**, 21722 (2017).
- [52] P. E. Blöchl, Projector augmented-wave method, *Phys. Rev. B* **50**, 17953 (1994).
- [53] J. P. Perdew, K. Burke, and M. Ernzerhof, Generalized Gradient Approximation Made Simple, *Phys. Rev. Lett.* **78**, 3865 (1997).
- [54] A. V. Krukau, O. A. Vydrov, A. F. Izmaylov, and G. E. Scuseria, Influence of the exchange screening parameter on the performance of screened hybrid functionals, *J. Chem. Phys.* **125**, 224106 (2006).
- [55] S. Grimme, Semiempirical GGA-type density functional constructed with a long-range dispersion correction, *J. Comput. Chem.* **27**, 1787 (2006).
- [56] G. Henkelman, B. P. Uberuaga, and H. Jónsson, A climbing image nudged elastic band method for finding saddle points and minimum energy paths, *J. Chem. Phys.* **113**, 9901 (2000).
- [57] L. E. Henrickson, Nonequilibrium photocurrent modeling in resonant tunneling photodetectors, *J. Appl. Phys.* **91**, 6273 (2002).
- [58] L. Zhang, K. Gong, J. Chen, L. Liu, Y. Zhu, D. Xiao, and H. Guo, Generation and transport of valley-polarized current in transition-metal dichalcogenides, *Phys. Rev. B* **90**, 195428 (2014).
- [59] J. Taylor, H. Guo, and J. Wang, *Ab initio* modeling of quantum transport properties of molecular electronic devices, *Phys. Rev. B* **63**, 245407 (2001).
- [60] Y. Q. Xie, L. Zhang, Y. Zhu, L. Liu, and H. Guo, Photogalvanic effect in monolayer black phosphorus, *Nanotechnology* **26**, 455202 (2015).
- [61] Y. Z. Luo, Y. B. Hu, and Y. Q. Xie, Highly polarization-sensitive, visible-blind and self-powered ultraviolet photodetection based on two-dimensional wide bandgap semiconductors: A theoretical prediction, *J. Mater. Chem. A* **7**, 27503 (2019).
- [62] For details of the NanoDCAL quantum transport package, see <http://www.hzwtech.com>.
- [63] H. M. Hu and G. Ouyang, First-principles calculations of interface engineering for 2D α -In₂Se₃-based van der Waals multiferroic heterojunctions, *Appl. Surf. Sci.* **545**, 149024 (2021).
- [64] H. Yang, M. Xiao, Y. Cui, L. Pan, K. Zhao, and Z. Wei, Nonvolatile memristor based on heterostructure of 2D room-temperature ferroelectric α -In₂Se₃ and WSe₂, *Sci. China. Inf. Sci.* **62**, 220404 (2019).
- [65] Y. Lu and J. H. Warner, Synthesis and applications of wide bandgap 2D layered semiconductors reaching the green and blue wavelengths, *ACS Appl. Electron. Mater.* **2**, 1777 (2020).
- [66] L. Tong, X. Y. Huang, P. Wang, L. Ye, M. Peng, L. C. An, Q. D. Sun, Y. Zhang, G. M. Yang, Z. Li, F. Zhong, F. Wang, Y. X. Wang, M. Motlag, W. Z. Wu, G. J. Cheng, and W. D. Hu, Stable mid-infrared polarization imaging based on quasi-2D tellurium at room temperature, *Nat. Commun.* **11**, 2308 (2020).
- [67] J. Bullock, M. Amani, J. Cho, Y. Z. Chen, G. H. Ahn, V. Adinolfi, V. R. Shrestha, Y. Gao, K. B. Crozier, Y. L. Chueh, and A. Javey, Polarization-resolved black phosphorus/molybdenum disulfide mid-wave infrared photodiodes with high detectivity at room temperature, *Nat. Photonics* **12**, 601 (2018).
- [68] R. Huang, D. H. Lin, J. Y. Liu, C. Y. Wu, D. Wu, and L. B. Luo, Nanochannel-confined growth of crystallographically orientated perovskite nanowire arrays for polarization-sensitive photodetector application, *Sci. China Mater.* **64**, 2497 (2021).
- [69] J. Qiao, F. Feng, Z. M. Wang, M. Y. Shen, G. P. Zhang, X. C. Yuan, and M. G. Somekh, Highly in-plane anisotropic two-dimensional ternary Ta₂NiSe₅ for polarization-sensitive photodetectors, *ACS Appl. Mater. Interfaces* **13**, 17948 (2021).

- [70] Z. H. Ren, P. Wang, K. Zhang, W. H. Ran, J. H. Yang, Y. Y. Liu, Z. Lou, G. Z. Shen, and Z. M. Wei, Short-wave near-infrared polarization sensitive photodetector based on GaSb nanowire, *IEEE Electron Device Lett.* **42**, 549 (2021).
- [71] P. K. Venuthurumilli, P. D. Ye, and X. F. Xu, Plasmonic resonance enhanced polarization-sensitive photodetection by black phosphorus in near infrared, *ACS Nano* **12**, 4861 (2018).
- [72] Y. Xin, X. X. Wang, Z. Chen, D. Weller, Y. Y. Wang, L. J. Shi, X. Ma, C. J. Ding, W. Li, S. Guo, and R. B. Liu, Polarization-sensitive self-powered type-II GeSe/MoS₂ van der Waals heterojunction photodetector, *ACS Appl. Mater. Inter.* **12**, 15406 (2020).
- [73] J. X. Xiong, Y. M. Sun, L. W. Wu, W. Z. Wang, W. Gao, N. J. Huo, and J. B. Li, High performance self-driven polarization-sensitive photodetectors based on GeAs/InSe heterojunction, *Adv. Opt. Mater.* **9**, 2101017 (2021).
- [74] Y. S. Yang, S. C. Liu, X. Wang, Z. B. Li, Y. Zhang, G. M. Zhang, D. J. Xue, and J. S. Hu, Polarization-sensitive ultraviolet photodetection of anisotropic 2D GeS₂, *Adv. Funct. Mater.* **29**, 1900411 (2019).
- [75] N. Zuo, A. M. Nie, C. G. Hu, W. F. Shen, B. Jin, X. Z. Hu, Z. Y. Liu, X. Zhou, and T. Y. Zhai, Synergistic additive-assisted growth of 2D ternary In₂SnS₄ with giant gate-tunable polarization-sensitive photoresponse, *Small* **17**, 2008078 (2021).
- [76] C. Ma, S. F. Yuan, P. Cheung, K. J. Watanabe, T. Taniguchi, F. Zhang, and F. N. Xia, Intelligent infrared sensing enabled by tunable moiré quantum geometry, *Nature* **604**, 266 (2022).
- [77] S. Dhara, E. J. Mele, and R. Agarwal, Voltage-tunable circular photogalvanic effect in silicon nanowires, *Science* **349**, 726 (2015).
- [78] J. Quereda, J. Hidding, T. S. Ghiasi, B. J. van Wees, C. H. van der Wal, and M. H. D. Guimarães, The role of device asymmetries and schottky barriers on the helicity-dependent photoresponse of 2D phototransistors, *Npj 2D Mater. Appl.* **5**, 13 (2021).
- [79] M. Nakamura, H. Hatada, Y. Kaneko, N. Ogawa, Y. Tokura, and M. Kawasaki, Impact of electrodes on the extraction of shift current from a ferroelectric semiconductor SbSI, *Appl. Phys. Lett.* **113**, 232901 (2018).
- [80] D. Huo, Y. S. Bai, X. Y. Lin, J. H. Deng, Z. M. Pan, C. Zhu, C. S. Liu, H. Y. Yu, and C. D. Zhang, Tuning of the valley structures in monolayer In₂Se₃/WSe₂ heterostructures via ferroelectricity, *Nano Lett.* **22**, 7261 (2022).
- [81] J. H. Zou, Y. Z. Ke, X. Y. Zhou, Y. X. Huang, W. Du, L. Lin, S. Y. Wei, L. Z. Luo, H. Z. Liu, C. L. Li, K. Shen, A. Ren, and J. Wu, Broadband visible-near infrared two-dimensional WSe₂/In₂Se₃ photodetector for underwater optical communications, *Adv. Opt. Mater.* **10**, 2200143 (2022).
- [82] Y. Li, C. Chen, W. Li, X. Y. Mao, H. Liu, J. Y. Xiang, A. M. Nie, Z. Y. Liu, W. G. Zhu, and H. L. Zeng, Orthogonal electric control of the out-of-plane field-effect in 2D ferroelectric α -In₂Se₃, *Adv. Electron. Mater.* **6**, 2000061 (2022).
- [83] J. Wang, C. L. Liu, L. B. Zhang, J. Chen, J. Chen, F. L. Yu, Z. Y. Zhao, W. W. Tang, X. Li, S. Zhang, G. H. Li, L. Wang, Y. Cheng, and X. S. Chen, Selective enhancement of photoresponse with ferroelectric-controlled BP/In₂Se₃ vdW heterojunction, *Adv. Sci.* **10**, 2205813 (2023).
- [84] M. Nakamura, S. Horiuchi, F. Kagawa, N. Ogawa, T. Kurumaji, Y. Tokura, and M. Kawasaki, Shift current photovoltaic effect in a ferroelectric charge-transfer complex, *Nat. Commun.* **8**, 281 (2017).